

Nonlinear Optical Radiation of a Lithium Niobate Microcavity

Yuan-Hao Yang^{1,4,§}, Xin-Biao Xu^{1,4,§}, Jia-Qi Wang^{1,4}, Mai Zhang^{1,4}, Ming Li^{1,4,*}, Zheng-Xu Zhu^{1,4}, Zhu-Bo Wang^{1,4}, Chun-Hua Dong^{1,4}, Wei Fang^{3,5}, Huakang Yu^{2,†}, Guang-Can Guo^{1,4}, and Chang-Ling Zou^{1,4,‡}

¹*CAS Key Laboratory of Quantum Information, University of Science and Technology of China, Hefei, Anhui 230026, People's Republic of China*

²*School of Physics and Optoelectronics, South China University of Technology, Guangzhou 510460, People's Republic of China*

³*Interdisciplinary Center for Quantum Information, State Key Laboratory of Modern Optical Instrumentation, College of Optical Science and Engineering, Zhejiang University, Hangzhou 310027, China*

⁴*CAS Center For Excellence in Quantum Information and Quantum Physics, University of Science and Technology of China, Hefei, Anhui 230026, People's Republic of China*

⁵*Intelligent Optics & Photonics Research Center, Jiaxing Research Institute Zhejiang University, Jiaxing 314000, China*



(Received 25 April 2022; revised 15 February 2023; accepted 23 February 2023; published 27 March 2023)

The nonlinear coupling between on-chip confined optical modes and free-space continuum modes is investigated. The radiation of second-harmonic wave due to the pump fields in integrated lithium niobate microcavities is experimentally observed. The mechanism of nonlinear optical radiation (NOR) is further verified by demonstrating the reversal process of NOR, i.e., the difference frequency generation between a free-space input and an on-chip pump field. The revealed mechanism of NOR is universal for all dielectric photonic integrated devices, which indicates unavoidable extra energy leakage channels of optical micro- and nanostructures, and also enables an alternative approach for spatial engineering of optical fields and light sources. For example, benefited from the phase-matching-free nature of NOR, an integrated atomic gas sensor for the absorption spectroscopy of Rb atoms is built.

DOI: 10.1103/PhysRevApplied.19.034087

I. INTRODUCTION

Cavity-enhanced nonlinear photonic devices offer a compact solution for efficient frequency conversion under low pump power owing to their small mode volume and high-quality factor (Q) [1–6]. In particular, the chip-integrated optical microcavity, which benefits from the high flexibility in dispersion engineering, enables significant nonlinear optical effects among multiple resonant modes with distinct wavelengths by $\chi^{(2)}$ and $\chi^{(3)}$ processes [7,8], as well as Raman and Brillouin scattering [9–11]. Over the past decades, the preparation and micro- and nanofabrication techniques of thin-film optical materials with high nonlinear susceptibility, such as aluminum nitride [12–16], gallium nitride [17–20], gallium arsenide [21–23], and lithium niobate (LN) [24–32], have been well developed, making integrated microcavities with a Q larger than 10^7 obtainable. As a result, an unprecedented

conversion efficiency $5 \times 10^4 \text{ W}^{-1}$ of second-harmonic generation (SHG) and ultralow-threshold optical parametric oscillators have been demonstrated in thin-film LN microcavities [33,34].

Despite the excellent performance of on-chip nonlinear optical devices, experimental studies are restricted to guided modes within integrated photonic circuits. These processes require critical phase-matching conditions [15, 16,35] and specially designed mode converters [36–41] for further free-space applications [42,43]. From the fundamental view of nonlinear optics, the in-plane guided modes also directly couple to the continuum modes in free space via the nonlinear susceptibility of materials. As a result, guided photons can radiate to free space by nonlinear conversion processes, which have long been neglected in integrated nonlinear photonics.

In this paper, an effect of nonlinear optical radiation (NOR) is theoretically investigated and experimentally observed. By simultaneously exciting counterpropagating resonant modes in integrated LN microrings, the NOR due to SHG process is collected in free space. Compared with the conventional doubly resonant SHG process between confined modes on a chip, the NOR is independent of

*lmwin@ustc.edu.cn

†hkyu@scut.edu.cn

‡clzou321@ustc.edu.cn

§These two authors contributed equally to this work.

the stringent structure for the phase-matching condition and is observed over a bandwidth of 130 nm (limited by tuning range of pump laser). The verified mechanism of NOR promises a nonlinear interface between integrated photonic structure and free space, and allows the construction of structural optical fields through engineering the pump field distribution and nonlinear susceptibility of on-chip structures. Our study also implies an ultimate limitation of optical quality factors of on-chip microresonators, which is appealing for the careful evaluation of NOR when designing photonic devices.

II. PRINCIPLE

The mechanism of NOR for a $\chi^{(2)}$ microcavity is illustrated in Fig. 1. NOR originates from the nonlinear coupling between the on-chip resonant modes $a_{1,2}$ and continuum modes b_k in free space. The interaction Hamiltonian governed by the three-wave mixing follows

$$H_{\text{nl}} = \sum_k g_k a_1 a_2 b_k^\dagger + g_k^* a_1^\dagger a_2^\dagger b_k, \quad (1)$$

where \mathbf{k} is the wave vector of the free-space mode and

$$g_k = 3 \int \chi^{(2)}(\mathbf{r}) \psi_1(\mathbf{r}) \psi_2(\mathbf{r}) E_k e^{-i\mathbf{k}\cdot\mathbf{r}} d\mathbf{r} \quad (2)$$

is the nonlinear coupling strength. Here, $\psi_{1,2}$ is the mode field distribution for the confined mode on the chip, E_k is the normalized amplitude of the continuum mode in free space, and $\chi^{(2)}(\mathbf{r})$ is the distribution of nonlinear susceptibility. Even though the cavity modes a_j constrained by the Helmholtz equation are quasiorthogonal to the free-space modes, the nonlinear response of the cavity material breaks such orthogonality and leads to nonzero g_k .

For a rotational-symmetric microring resonator, we transform the wave vector and position to the sphere coordinate and cylindrical coordinate by $\mathbf{k} = (k_x, k_y, k_z) = (k \sin \theta_k \cos \phi_k, k \sin \theta_k \sin \phi_k, k \cos \theta_k)$ and $\mathbf{r} = (r \cos \phi_r, r \sin \phi_r, h)$, respectively. Due to the rotational symmetry of the ring cavity, we have $\psi_j(\mathbf{r}) = E_j(r, h) e^{im_j \phi_r}$, with m_j being the mode index. For simplicity, we assume a uniform transverse-mode distribution of $a_{1,2}$ with $E_1 \approx E_2 = E_0$ and an isotropic material nonlinear susceptibility. For a cavity with waveguide width much smaller than the ring radius, $w \ll R$, we can derive (Appendix A)

$$g_k \propto \chi^{(2)} \int_R^{R+w} r dr J_{-(m_1+m_2)} \left(\frac{-\omega_k \sin \theta_k r}{c} \right). \quad (3)$$

Here, $J_{-(m_1+m_2)}(-\omega_k \sin \theta_k r / c)$ is an $-(m_1+m_2)$ th order Bessel function. This indicates that the nonlinear coupling strength should depend on the mode index sum. The microring cavity is special in that it supports two families of degenerate resonant modes with opposite signs

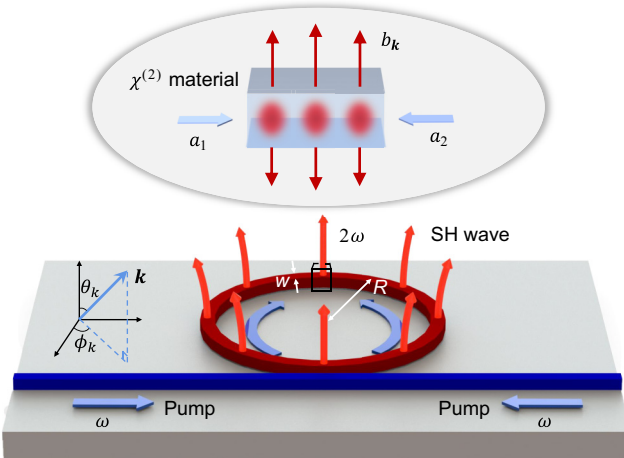


FIG. 1. Schematic illustration of the NOR process. The blue arrows indicate counterpropagating pump lasers (frequency ω), while the red arrows indicate vertically radiated second-harmonic light (frequency 2ω). The inset shows the details of the nonlinear interaction between guided modes and free-space continuum modes at the cross section of the microring.

of m_j . For modes propagating along the same direction, $|m_1 + m_2| \gg \omega_k \sin \theta_k r'$ for $\theta_k \ll 1$, and g_k is relatively small. For counterpropagating modes, $|m_1 + m_2|$ can be made to a small number and one obtains a much larger g_k , which is beneficial for experimental observation of NOR.

The amplitude of the radiation field at position \mathbf{r}' can be calculated by

$$E(\mathbf{r}') = \int_{\mathbf{k}} dk \sqrt{\frac{\hbar \omega_k}{2\epsilon_0 V}} g_k e^{i\mathbf{k}\cdot\mathbf{r}'} \alpha_1 \alpha_2, \quad (4)$$

where $\alpha_{1,2} = \sqrt{4P_{\text{pump},1,2}Q^2/\hbar\omega^2Q_{\text{ext}}}$ is the intracavity photon-number amplitude of mode $a_{1,2}$. Thus, for $\alpha_1 \approx \alpha_2$ and critical-coupled microring $Q_{\text{ext}} = 2Q$, the radiation amplitude $E \propto g_k P_{\text{pump}} Q$, and the radiation power $P_{\text{NOR}} \propto |E|^2$.

III. EXPERIMENTAL RESULTS OF NOR

The NOR mechanism is investigated by integrated LN microring cavities (Appendix C) by the experimental setup shown in Fig. 2(a). The devices are driven by a continuous-wave telecom laser (1550 nm) from two opposite directions simultaneously, using a 50:50 fiber beam-splitter fiber to divide the laser into two paths. Two fiber circulators are introduced in each path for separating and detecting transmitted and reflected signals. Fiber polarization controllers are adjusted for maximum coupling efficiencies to the transverse-electric (TE) modes of the integrated devices. The free-space radiation of the microcavity is collected by an objective lens, with 10% of the signal sent to the CCD for real-time imaging, while the rest (90%) of

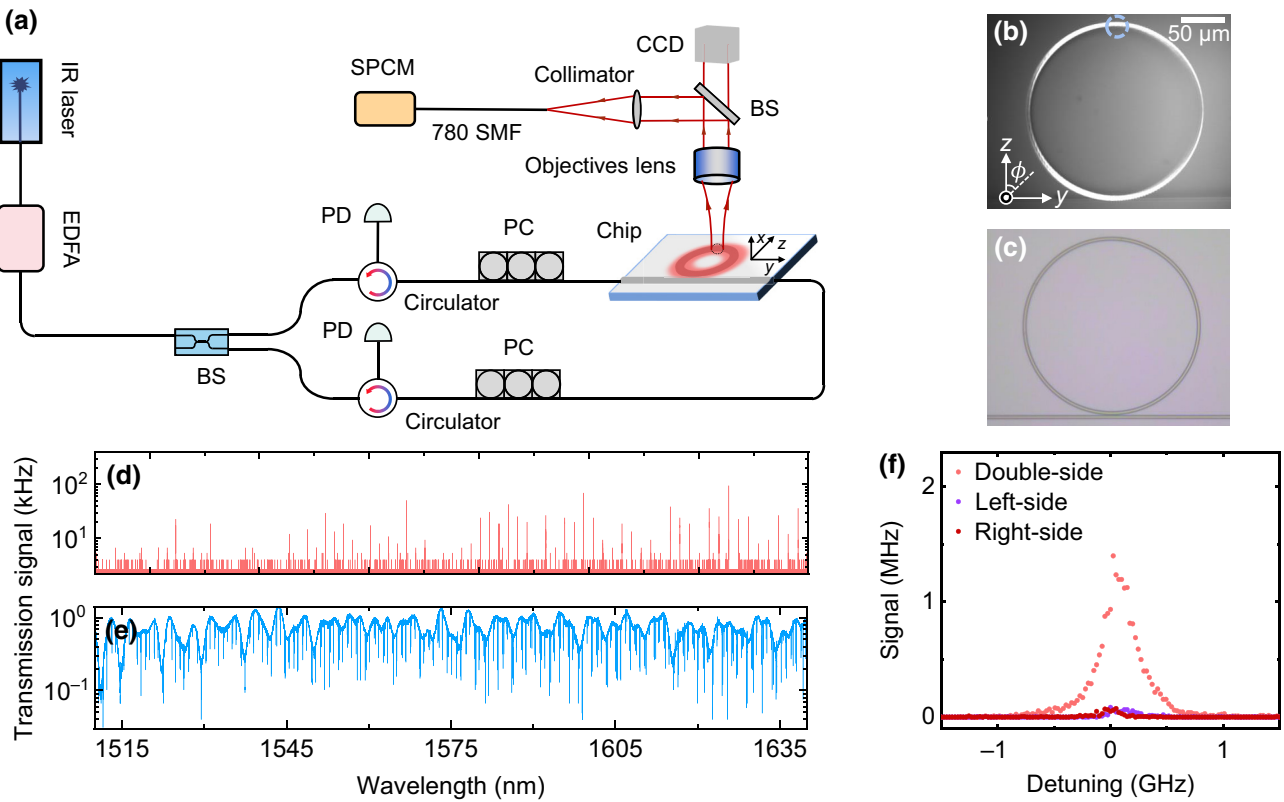


FIG. 2. (a) Experimental setup. The pump laser is split by a 50:50 BS and launched to the chip from two directions. The radiated light is collected by an objective lens with NA of 0.42. IR laser, infrared laser; EDFA, erbium-doped fiber amplifier; BS, beam splitter; PC, polarization controller; PD, photodetector; SPCM, single-photon-counting module; 780 SMF, 780-nm single mode fiber. The NOR signal is coupled into a standard 780 SMF, which naturally filters the scattering of the telecom pump. The axes on the chip denote crystal orientations of the thin-film LN, which is corresponding to the axes in (b). (b),(c) The real-time microscope image of the microring with and without double-side pump. (d),(e) The detected NOR signal and transmission spectra of pump, respectively. (f) The comparison between double-side and single-side pump. Purple and dark red dots represent left- and right-side pump situations, and red dots represent double-side pump situation. Here, $P_{\text{pump, double}} = P_{\text{pump, left}} + P_{\text{pump, right}}$.

the signal is directed to a single mode fiber (SMF) through a collimator and then fed into a single-photon-counting module (SPCM).

When scanning the pump lasers, we observe the periodic shining of the microring from the CCD, which responds only to visible light. Shown in Fig. 2(b) is an image of the device obtained from the CCD, which is obviously lit only when the pump laser is on resonance with the microring, while the radiation of the waveguide is invisible. In addition, the radiated visible photons were collected from a small section of the microring, as indicated by the blue circle in Fig. 2(b). The photons are detected by a SPCM when the wavelength of the telecom laser scans from 1510 to 1640 nm with a scanning speed of 0.5 nm/s. The resulting spectra of the counts and the transmitted telecom pump laser are shown in Figs. 2(d) and 2(e). The aligned peaks of the visible photons and the dips of the pump laser in the spectra (Appendix C) confirm that the radiation occurs for all microring modes when the pump laser is on resonance and indicates the broadband nature of NOR.

To distinguish the visible radiation from the linear scattering of the unexpected SHG generated by guided modes in the microring and waveguide due to surface roughness, the NOR process enjoys the following unique features: (i) The radiation is broadband over a bandwidth exceeding 130 nm. The large bandwidth indicates that the NOR is free of phase-matching engineering, in contrast to the narrow bandwidth of on-chip SHG. (ii) As shown in Fig. 2(f), the radiation power of the double-side pump is much larger than that of the single-side pump, which is theoretically predicted with Eq. (3). (iii) The radiation from the microring is $\propto \cos^4 \phi$ along the azimuthal angle ϕ for the x -cut LN and TE modes due to the variation of the $\chi^{(2)}$ nonlinear susceptibility tensor (Appendix B). It is the brightest in the upper and lower parts where the largest second-order nonlinear coefficients ($d_{33} = -27 \text{ pm/V}$) can be accessed. In contrast, the surface roughness induced scattering of the microring should produce a near-uniform radiation pattern.

According to Eq. (4), the NOR power should follow a quadratic relationship with the input pump power,

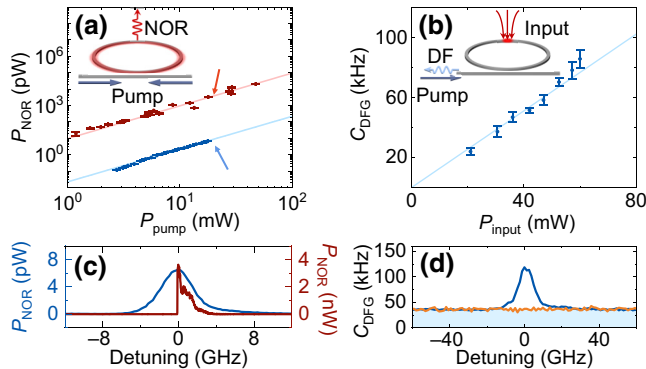


FIG. 3. (a),(b) Input-output power dependency of NOR and DFG, respectively. The dots show the experimental results while the solid lines represent quadratic and linear fittings. The insets illustrate the inputs and outputs for NOR and DFG, respectively. C_{DFG} is short for counting rate of DFG signal. The colors red and blue represent the results of devices *A* and *B*, respectively. (c) The spectrum of NOR when sweeping the pump frequency across cavity resonance, with P_{pump} shown in (a) with arrows. (d) Spectra of the DFG signal when sweeping the frequency of visible input, with $P_{\text{input}} = 60.0$ mW. Blue and orange lines are the results for input focused on microring and waveguide, respectively, and shadow indicates the background noise level when visible input is absent.

similar to the case of on-chip SHG. As shown in Fig. 3(a), we compare the power relationship of two different LN microcavities. The red (blue) dots and line represent the device marked as device *A* (*B*) with loaded Q factor of 8.05×10^5 (6.99×10^4). Each data point in Fig. 3(a) represents the fitted peak value of the collected radiation spectra for a given pump power. Typical spectra of the NOR for *A* and *B* [marked with blue and red arrows in Fig. 3(a)] are shown in Fig. 3(c). The power of NOR (P_{NOR}) increases quadratically with the pump power for both devices *A* and *B*. By fitting the experimental data, we obtain $P_{\text{NOR}}/P_{\text{pump}}^2 = 9.53 \pm 0.49$ and $(2.21 \pm 0.03) \times 10^{-2}$ pW mW $^{-2}$ for devices *A* and *B*, respectively. Device *A* experimentally shows a P_{NOR} over 400 times larger than device *B* with a higher Q . According to the experimental parameters of our devices, including Q factors, sizes of the microrings, and NA of the objective lens, our theory (Appendix A) predicts NOR efficiencies $P_{\text{NOR}}/P_{\text{pump}}^2 = 16.06$ and 0.35×10^{-2} pW/mW 2 for the devices *A* and *B*, respectively, whose numbers are on the same order of magnitude as the experimental values.

IV. REVERSAL OF NOR

The intrinsic coherence property of the nonlinear coupling in Eq. (1) also supports a reversal process of NOR, i.e., the difference frequency generation (DFG) from free-space photons to on-chip guided photons. Therefore, we design and carry out the experiment by injecting

visible laser into the microring, as schematically illustrated by the inset of Fig. 3(b). DFG is realized by reversing the setup of the collection of visible radiation in Fig. 2(b), and sending visible laser into the 780-nm SMF. Then, a vertically input visible photon could be converted to two counterpropagating telecom photons in the microring, with the conversion stimulated by a pump laser. Due to the energy-conservation condition, the frequency of the DFG signal is $\omega_{\text{DF}} = \omega_{\text{input}} - \omega_{\text{pump}}$, so the process is only efficient when ω_{DF} meets a resonant mode. We expect efficient DFG for $\Delta = \omega_{\text{input}} - 2\omega_{\text{pump}}$ being integer multiples of the microring free spectral range (FSR) Ω up to a small cavity dispersion. To avoid the noisy background due to the backscattering of pump in the microring, we investigate the nondegenerate DFG with $\Delta \approx 600$ GHz, which corresponds to two FSRs and is large enough for high-performance filtering. We cascade four bandpass filters to achieve high signal-to-noise ratio, with the signal and background noise shown in Fig. 3(d).

Then, the dependence of nondegenerate DFG signal on the power of the visible input is investigated, while fixing both the power and frequency of the telecom pump on resonance with the microring. Considering that the LN device on the sapphire substrate (device *B*) suffers less photorefractive and thermal effects than that on the silica substrate (device *A*), it is easier to fix the pump frequency stably on resonance. Thus, we choose device *B* to further characterize the DFG to verify the NOR mechanism. The blue line in Fig. 3(d) shows a typical spectrum of DFG obtained by fixing the on-chip pump power at 10.5 mW, and sweeping the detuning of visible input laser with a sweeping speed of 1 nm/s and a power of $P_{\text{input}} = 60$ mW. Comparing the results for the free-space visible input focusing on microring and waveguide, we come to the conclusion that DFG is enhanced by the cavity while the signal generated in bus waveguide is negligible. For a given P_{input} , the DFG signal can be deduced by subtracting the background noise from the peak of spectrum. The linear relationship between the DFG signal and P_{input} in Fig. 3(b) confirms the coherent frequency conversion between the free-space light and the on-chip guided modes, which not only validates the mechanism of NOR, but also promises potential applications for detecting free-space radiation.

V. APPLICATION

The demonstrated NOR provides a broadband nonlinear chip-to-free-space interface and offers opportunities for practical applications of photonic chips. For instance, by leveraging the NOR effect of a well-developed on-chip optical soliton microcomb [3,4], radiated visible soliton pulses can be used to probe the gas or liquid sample around the chip. Here, we conduct a proof-of-principle application of the NOR for atomic gas sensing, as shown in Fig. 4(a). By placing a glass cell filling with sample

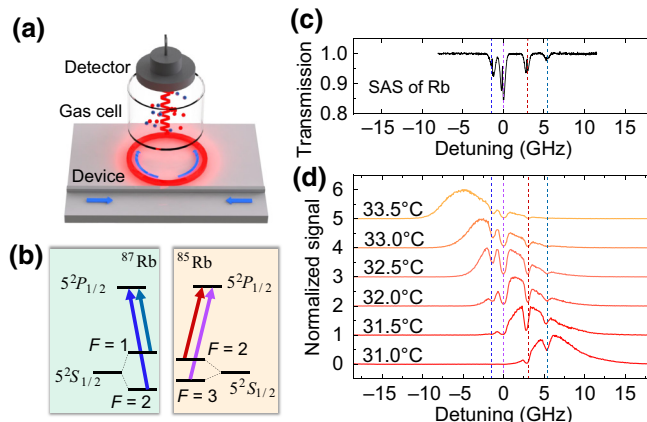


FIG. 4. (a) Illustration of multicomponent gas sensor based on NOR. (b) D2 transitions of ⁸⁵Rb and ⁸⁷Rb atoms. (c) Saturation absorption spectrum (SAS) of rubidium gas. (d) Tunability of NOR under thermal control of the microcavity. The bandwidth of the device covers all transition lines, shown by the vertical dashed lines.

atoms above the chip, the absorption spectra are obtained by measuring the transmitted NOR signal. The absorption spectra of two isotopes of rubidium atom, i.e., ⁸⁵Rb and ⁸⁷Rb, which have been extensively investigated in quantum information processing, atomic clock, and precision measurement [42,44–46], are studied when the frequency of NOR matches their D2 transition lines [Fig. 4(b)].

The phase-matching-free nature of NOR allows broadband scanning of the spectrum by simply tuning the telecom resonant mode, which otherwise would be difficult for SHG between guided modes and requires an additional chip-fiber or chip-to-free-space coupling apparatus. The microring cavity is finely tuned to match the transition line around 780.25 nm by an off-chip heater. We choose device *B* to detect the transmission spectra due to its lower *Q* factor and larger linewidth of the resonance mode, which helped to cover the transition lines. The normalized transmission spectra in Fig. 4(d) show four dips that could be identified as the transitions of ⁸⁵Rb and ⁸⁷Rb by comparison to the reference saturated absorption spectrum (SAS) [Fig. 4(c)], measured in another system specially built for probing SAS with the same cell]. By gradually changing the temperature of the heater [Fig. 4(d)], the NOR peak shifted step by step, which indicates the tunability and controllability of NOR in spectroscopy.

In the current device, the performance of the gas sensor is limited by the radiation efficiency. As verified by the two devices in Fig. 3(a), the NOR efficiency of SHG scales quadratically with the *Q* of microring modes. Therefore, we expect a higher NOR efficiency in LN microcavities with higher *Q*. For a state-of-the-art *Q* > 10⁷, the radiation efficiency from the whole microring reaches 10⁶ pW/mW², i.e., approximately 10% of the intracavity energy is radiated through NOR for *P*_{pump} = 100 mW, is

predicted. Therefore, the NOR holds the potential for practical applications, to realize high-precision spectroscopy and sensing [47,48], as well as optical clock by referencing atomic transitions [42,44].

VI. CONCLUSION

In conclusion, the nonlinear optical radiation of integrated photonic devices is theoretically and experimentally revealed by investigating the free-space second-harmonic radiation of LN microring cavities. The nonlinear optical radiation and its reversal free-space-to-chip nonlinear frequency conversion are verified. It is worth noting that second-harmonic radiation from guided modes into unguided modes has been observed in bulky waveguides decades ago [49], which is also known as Cerenkov second-harmonic radiation. However, its mechanism is different from our work, because the Cerenkov radiation and the traveling-wave pump should satisfy the phase-matching condition. Due to the enhanced nonlinear optical interactions for integrated devices, the NOR is significant and universal and can be extended to other nonlinear optical processes and materials. Therefore, the mechanism not only promises applications for interfacing free space and photonic chips, but is also appealing for more careful investigation and design of photonic devices, especially for quantum devices and precision measurement instruments, in which the nonlinear optical radiation might introduce non-negligible and unavoidable noise photons.

ACKNOWLEDGMENTS

This work is funded by the National Key Research and Development Program (Grant No. 2018YFA0306200), the National Natural Science Foundation of China (Grants No. 11874342, No. 11904316, No. 11922411, No. 12104441, No. 11934012, No. 91850107, No. 12174116, and No. U21A6006), Anhui Provincial Natural Science Foundation (Grants No. 2008085QA34 and No. 2108085MA22), Guangdong Innovative and Entrepreneurial Research Team Program (Grant No. 2016ZT06C594), Science and Technology Project of Guangdong (2020B010190001). It is also supported by the Fundamental Research Funds for the Central Universities, USTC Research Funds of the Double First-Class Initiative, and the State Key Laboratory of Advanced Optical Communication Systems and Networks, China. This work is partially carried out at the USTC Center for Micro and Nanoscale Research and Fabrication.

APPENDIX A: NONLINEAR OPTICAL RADIATION OF THE $\chi^{(2)}$ CAVITY

1. Interaction Hamiltonian

We consider the three-wave mixing between two localized cavity modes $a_{1,2}$ on a photonic chip and the

continuous modes $b_{\mathbf{k}}$ in free space, with \mathbf{k} denoting the wave vector of the continuous mode. The fields of these modes are quantized as

$$\mathbf{E}_j(\mathbf{r}, t) = a_j \psi_j(\mathbf{r}) e^{-i\omega_j t} + a_j^\dagger \psi_j^*(\mathbf{r}) e^{i\omega_j t}, \quad (\text{A1})$$

$$\mathbf{E}_{\mathbf{k}}(\mathbf{r}, t) = \hat{\epsilon}_{\mathbf{k}} \epsilon_{\mathbf{k}} b_{\mathbf{k}} e^{-i\omega_k t + i\mathbf{k} \cdot \mathbf{r}} + \hat{\epsilon}_{\mathbf{k}} \epsilon_{\mathbf{k}} b_{\mathbf{k}}^\dagger e^{i\omega_k t - i\mathbf{k} \cdot \mathbf{r}}, \quad (\text{A2})$$

where $\hat{\epsilon}_{\mathbf{k}}$ is the polarization of the \mathbf{k} wave ($\hat{\epsilon}_{\mathbf{k}} \cdot \mathbf{k} = 0$), and the fields $\psi_j(\mathbf{r})$ and $\epsilon_{\mathbf{k}}$ fulfill the normalization condition

$$\epsilon_0 \int \epsilon(\mathbf{r}) |\psi_j(\mathbf{r})|^2 d\mathbf{r} = \frac{\hbar\omega_j}{2}, \quad (\text{A3})$$

$$\epsilon_0 \epsilon_{\mathbf{k}}^2 V = \frac{\hbar\omega_k}{2}, \quad (\text{A4})$$

where ϵ_0 is the vacuum permittivity, $\epsilon(\mathbf{r})$ is the relative permittivity, V is the volume of quantization, and $\omega_k/|\mathbf{k}| = c$. The nonlinear interaction is induced by the $\chi^{(2)}$ nonlinear susceptibility tensor, with an interaction Hamiltonian of

$$\begin{aligned} H &= \frac{1}{2} \int \mathbf{E}(\mathbf{r}) \cdot \mathbf{D}_{\text{nl}}(\mathbf{r}) d\mathbf{r}, \\ &= \frac{1}{2} \epsilon_0 \int \mathbf{E}(\mathbf{r}) \cdot [\chi^{(2)}(\mathbf{r}) \cdot \mathbf{E}(\mathbf{r}) \mathbf{E}(\mathbf{r})] d\mathbf{r}. \end{aligned} \quad (\text{A5})$$

Here the electric field $\mathbf{E}(\mathbf{r}) = \mathbf{E}_1(\mathbf{r}, t) + \mathbf{E}_2(\mathbf{r}, t) + \mathbf{E}_{\mathbf{k}}(\mathbf{r}, t)$, is the nonlinearity-induced electric displacement vector.

By substituting the electric field into Eq. (A5) and discarding the high-frequency term, we arrive at the interaction Hamiltonian describing the sum-frequency generation of the two guided modes to the space mode

$$\begin{aligned} H_{\text{nl}} &= \sum_{\mathbf{k}} \frac{3}{2} \epsilon_0 \int \chi^{(2)}(\mathbf{r}) \psi_1(\mathbf{r}) \psi_2(\mathbf{r}) \hat{\epsilon}_{\mathbf{k}} \epsilon_{\mathbf{k}} \\ &\quad \times e^{-i(2\omega_a - \omega_k)t - i\mathbf{k} \cdot \mathbf{r}} d\mathbf{r} a^2 b_{\mathbf{k}}^\dagger + \text{h.c.} \\ &= \sum_{\mathbf{k}} g_{\mathbf{k}} a_1 a_2 b_{\mathbf{k}}^\dagger e^{-i(\omega_1 + \omega_2 - \omega_k)t} \\ &\quad + g_{\mathbf{k}}^* a_1^\dagger a_2^\dagger b_{\mathbf{k}} e^{i(\omega_1 + \omega_2 - \omega_k)t}. \end{aligned} \quad (\text{A6})$$

For an isotropic nonlinear response $\chi^{(2)}$ of the microcavity dielectric material, we have

$$\begin{aligned} g_{\mathbf{k}} &= \frac{6}{2} \sqrt{\frac{\hbar\omega_k \epsilon_0}{2V}} \int \chi^{(2)} \psi_1(\mathbf{r}) \psi_2(\mathbf{r}) \hat{\epsilon}_{\mathbf{k},l} e^{-i\mathbf{k} \cdot \mathbf{r}} d\mathbf{r}, \\ &= \int \chi^{(2)} g_{\mathbf{k}}(\mathbf{r}) \hat{\epsilon}_{\mathbf{k},l} e^{-i\mathbf{k} \cdot \mathbf{r}} d\mathbf{r}. \end{aligned} \quad (\text{A7})$$

2. Microring cavity

For rotational-symmetric microring resonator, we transform the wave vector and position to the sphere coordinate and cylindrical coordinate by $\mathbf{k} = (k_x, k_y, k_z) =$

$(k \sin \theta_k \cos \phi_k, k \sin \theta_k \sin \phi_k, k \cos \theta_k)$ and $\mathbf{r} = (r \cos \phi_r, r \sin \phi_r, h)$, respectively. Due to the rotational symmetry of the ring cavity, we have

$$\psi_j(\mathbf{r}) = E_j(r, h) e^{im_j \phi_r}, \quad (\text{A8})$$

where m_j is the mode index, which represents the orbit angular momentum. Then, for mode $a_{1,2}$ with a similar transverse distribution, $E_1 \approx E_2$ and

$$\begin{aligned} g_{\mathbf{k}} &= \frac{6}{2} \sqrt{\frac{\hbar\omega_k \epsilon_0}{2V}} \chi^{(2)} \iiint E^2(r, h) r dr dh d\phi_r \\ &\quad \times e^{i(m_1 + m_2)\phi_r} e^{-i(k_x r \cos \phi_r + k_y r \sin \phi_r + k_z h)}. \end{aligned} \quad (\text{A9})$$

For simplicity, we make another approximation that mode a has a uniform distribution, i.e., $E_j(r, h) = E_0$. According to the normalization condition

$$\epsilon_0 \epsilon_a \int r dr dh d\phi_r E_j^2 = \frac{\hbar\omega_j}{2}, \quad (\text{A10})$$

we have

$$E_0^2 = \frac{\hbar\omega_a}{4\pi \epsilon_0 \epsilon_a R S}, \quad (\text{A11})$$

for $w \ll R$, with R and S being the radius of the ring and mode area of the cross section, respectively. The coupling strength approximates to

$$\begin{aligned} g_{\mathbf{k}} &= \frac{6}{2} \sqrt{\frac{\hbar\omega_k \epsilon_0}{2V}} \chi^{(2)} \iiint E^2(r, h) r dr dh d\phi_r \\ &\quad \times e^{i(m_1 + m_2)\phi_r} e^{-i(k_x r \cos \phi_r + k_y r \sin \phi_r + k_z h)} \\ &= \frac{6}{2} \sqrt{\frac{\hbar\omega_k \epsilon_0}{2V}} \chi^{(2)} E^2 2\pi r e^{-i(m_1 + m_2)\pi/2} e^{i(m_1 + m_2)\phi_k} \\ &\quad (1 - e^{-ik_z h}) \\ &\quad \times \frac{1}{ik_z} \int_R^{R+w} r dr J_{-(m_1 + m_2)}(-k \sin \theta_k r). \end{aligned} \quad (\text{A12})$$

3. Radiation power

Denoting $A = a_1 a_2$, $\omega_A = \omega_1 + \omega_2$ and $m_A = m_1 + m_2$, the interaction Hamiltonian has a simple form

$$H_{\text{nl}} = \hbar \sum_j \int d\mathbf{k} g_j(\mathbf{k}) A b_{\mathbf{k}}^\dagger e^{-i(\omega_A - \omega_k)t} + \text{h.c.} \quad (\text{A13})$$

Following the standard treatment in quantum optics, we denote the cavity as the desired system and the continuum of modes as a reservoir. The density matrices of the whole system, cavity and reservoir are ρ_{AR} , ρ_A , and

ρ_R , respectively. The dynamics follow the Schrodinger equation

$$\frac{d}{dt}\rho_{AR} = -\frac{i}{\hbar}[H_{nl}, \rho_{AR}(t)], \quad (\text{A14})$$

with a solution of

$$\rho_{AR}(t) = \rho_{AR}(t_0) - \frac{i}{\hbar} \int_{t_0}^t [H_{nl}(t'), \rho_{AR}(t')] dt'. \quad (\text{A15})$$

Submit the solution back to the Schrodinger equation

$$\begin{aligned} \frac{d}{dt}\rho_{AR} &= -\frac{i}{\hbar}[H_{nl}(t'), \rho_{AR}(t_0)] \\ &\quad - \frac{1}{\hbar^2} \int_{t_0}^t [H_{nl}(t), [H_{nl}(t'), \rho_{AR}(t')]] dt'. \end{aligned} \quad (\text{A16})$$

For weak system-reservoir interactions, the correlation between the system and reservoir can be neglected, thus the Born approximation could be applied as

$$\rho_{AR}(t) = \rho_A(t) \otimes \rho_R(t_0). \quad (\text{A17})$$

Under the Markov approximation, the dynamics of the system can be derived as

$$\begin{aligned} \frac{d}{dt}\rho_A(t) &= -\frac{i}{\hbar}\text{Tr}_R[H_{nl}(t), \rho_A(t_0) \otimes \rho_R(t_0)] \\ &\quad - \frac{1}{\hbar^2} \text{Tr}_R \int_{t_0}^t [H_{nl}(t), [H_{nl}(t'), \rho_A(t) \\ &\quad \otimes \rho_R(t_0)]] dt'. \end{aligned} \quad (\text{A18})$$

Submit Eqs. (A13)–(A18), then

$$\begin{aligned} \frac{d}{dt}\rho_A(t) &= -\sum_j \int dt' d\mathbf{k} |g_{k,j}|^2 [A^\dagger A \rho_A(t') - A \rho_A(t') A^\dagger] \\ &\quad \times e^{i(\omega_A - \omega_k)(t-t')} + \text{h.c.} \end{aligned} \quad (\text{A19})$$

Here,

$$\begin{aligned} g_{\mathbf{k}} &= \frac{6}{2} \sqrt{\frac{\hbar\omega_k\epsilon_0}{2V}} \chi^{(2)} E^2 \frac{1}{ik\cos\theta_k} (1 - e^{-ik\cos\theta_k h}) \\ &\quad \times e^{-im_A\pi/2} e^{im_A\phi_k} 2\pi \int_R^{R+w} r dr J_{-m_A}(-ksin\theta_k r), \end{aligned} \quad (\text{A20})$$

and

$$\begin{aligned} |g_{\mathbf{k}}|^2 &= (2\pi)^2 \frac{36\hbar\omega_k\epsilon_0}{8V} \chi^{(2)} E^4 \frac{1}{k^2\cos^2\theta_k} |1 - e^{-ik\cos\theta_k h}|^2 \\ &\quad \times \left[\int_R^{R+w} r dr J_{-m_A}(-ksin\theta_k r) \right]^2. \end{aligned} \quad (\text{A21})$$

The integration over \mathbf{k} is taken by

$$\sum_j \int d\mathbf{k} \rightarrow \frac{2V}{(2\pi)^3} \int_0^{2\pi} d\phi_k \int_0^\pi d\theta_k \sin\theta_k \int_0^\infty dk k^2 \quad (\text{A22})$$

$$\rightarrow \frac{2V}{c^3(2\pi)^3}$$

$$\times \int_0^{2\pi} d\phi_k \int_0^\pi d\theta_k \sin\theta_k \int_0^\infty d\omega_k \omega_k^2. \quad (\text{A23})$$

Then, the total decay rate is derived as

$$\begin{aligned} \kappa &= \frac{9\epsilon_0\omega_A}{2\pi c} \chi^{(2)} E^4 \int_0^{2\pi} d\phi_k \int_0^\pi d\theta_k \frac{\sin\theta_k}{\cos^2\theta_k} \\ &\quad \times |1 - e^{-i\omega_A \cos\theta_k h/c}|^2 \left[\int_R^{R+w} r dr J_{-m_A}(-\omega_A \sin\theta_k r/c) \right]^2 \\ &= \frac{9\epsilon_0\omega_A}{c} \chi^{(2)} E^4 \int_0^\pi d\theta_k \frac{\sin\theta_k}{\cos^2\theta_k} |1 - e^{-i\omega_A \cos\theta_k h/c}|^2 \\ &\quad \times \left[\int_R^{R+w} r dr J_{-m_A}(-\omega_A \sin\theta_k r/c) \right]^2 \\ &\approx \frac{9\hbar^2 \omega_a^2 \omega_A w^2 \chi^{(2)} 2}{16\pi^2 c \epsilon_0 \epsilon_a^2 A^2} \int_0^\pi d\theta_k \frac{\sin\theta_k}{\cos^2\theta_k} |1 - e^{-i\omega_A \cos\theta_k h/c}|^2 \\ &\quad \times [J_{-m_A}(-\omega_A \sin\theta_k R/c)]^2. \end{aligned} \quad (\text{A24})$$

For a selected solid angle of \mathbf{k} , we just change the integration range of θ_k . Then, the power of the radiation field is derived as

$$P_{\text{rad}} = 2\hbar\omega_A \kappa |\alpha_1 \alpha_2|^2. \quad (\text{A25})$$

In our experimental setup, we use an objective lens to collect NOR, and the collected power can be estimated as

$$P_{\text{col}} = \frac{\pi r^2}{2\pi R w} P'_{\text{rad}}, \quad (\text{A26})$$

where r is the radius of the collection area and w is the width of the microring. P'_{rad} is the radiation power within a certain degree corresponding to the NA of the collective lens, which can be numerically calculated by changing the range of integration in Eq. (A24).

APPENDIX B: LN WITH ANISOTROPIC NONLINEAR RESPONSE

The response of the polarizability due to $\chi^{(2)}$ in lithium niobate is written as

$$\begin{pmatrix} P_x \\ P_y \\ P_z \end{pmatrix} = 2 \times \begin{pmatrix} 0 & 0 & 0 & 0 & d_{31} & -d_{22} \\ -d_{22} & d_{22} & 0 & d_{31} & 0 & 0 \\ d_{31} & d_{31} & d_{33} & 0 & 0 & 0 \end{pmatrix} \times \begin{pmatrix} E_x^2 \\ E_y^2 \\ E_z^2 \\ 2E_xE_y \\ 2E_zE_x \\ 2E_xE_y \end{pmatrix}, \quad (\text{B1})$$

which leads to an interaction energy

$$\begin{aligned} U_{\text{nl}} &= \frac{\epsilon_0}{2} \sum_{j \in \{x,y,z\}} E_j \cdot P_j \\ &= \epsilon_0 [2E_x (d_{31}E_zE_x - d_{22}E_xE_y) \\ &\quad + E_y (-d_{22}E_x^2 + d_{22}E_y^2 + 2d_{31}E_xE_y) \\ &\quad + E_z (d_{31}E_x^2 + d_{31}E_y^2 + d_{33}E_z^2)] \\ &= \epsilon_0 [3d_{31}E_x^2E_z - 3d_{22}E_x^2E_y + d_{22}E_y^3 \\ &\quad + 2d_{31}E_xE_y^2 + d_{31}E_y^2E_z + d_{33}E_z^3]. \end{aligned} \quad (\text{B2})$$

This inhomogeneous response leads to an interaction strength of

$$\begin{aligned} g_{\mathbf{k},j} &= \frac{1}{2}\epsilon_0\sqrt{\frac{\hbar\omega_k}{2\epsilon_0V}} \int d\mathbf{r} e^{-i\mathbf{k}\cdot\mathbf{r}} \\ &\quad [3d_{31} (2u_xu_z\hat{\epsilon}_{\mathbf{k},x} + u_x^2\hat{\epsilon}_{\mathbf{k},z}) \\ &\quad - 3d_{22} (2u_xu_y\hat{\epsilon}_{\mathbf{k},x} + u_x^2\hat{\epsilon}_{\mathbf{k},y}) \\ &\quad + 3d_{22}u_y^2\hat{\epsilon}_{\mathbf{k},y} + 2d_{31} (2u_xu_y\hat{\epsilon}_{\mathbf{k},y} + u_y^2\hat{\epsilon}_{\mathbf{k},x}) \\ &\quad + d_{31} (2u_yu_z\hat{\epsilon}_{\mathbf{k},y} + u_y^2\hat{\epsilon}_{\mathbf{k},z}) + 3d_{33}u_z^2\hat{\epsilon}_{\mathbf{k},z}]. \end{aligned} \quad (\text{B3})$$

Considering all the continuous modes in free space, the total interaction Hamiltonian is written as

$$\begin{aligned} H_{\text{nl}} &= \sum_{j \in \{1,2\}} \int d\mathbf{k} g_{\mathbf{k}} a_1 a_2 b_{\mathbf{k}}^\dagger e^{-i(\omega_1+\omega_2-\omega_k)t} + \text{h.c.} \\ &= \frac{1}{2}\epsilon_0 \int \int d\mathbf{k} d\mathbf{r} \sqrt{\frac{\hbar\omega_k}{2\epsilon_0V}} e^{-i\mathbf{k}\cdot\mathbf{r}} a_1 a_2 b_{\mathbf{k}}^\dagger e^{-i(\omega_1+\omega_2-\omega_k)t} \end{aligned}$$

$$\begin{aligned} &\times [3d_{31} (2u_xu_z\hat{\epsilon}_{\mathbf{k},x} + u_x^2\hat{\epsilon}_{\mathbf{k},z}) \\ &- 3d_{22} (2u_xu_y\hat{\epsilon}_{\mathbf{k},x} + u_x^2\hat{\epsilon}_{\mathbf{k},y}) \\ &+ 3d_{22}u_y^2\hat{\epsilon}_{\mathbf{k},y} + 2d_{31} (2u_xu_y\hat{\epsilon}_{\mathbf{k},y} + u_y^2\hat{\epsilon}_{\mathbf{k},x}) \\ &+ d_{31} (2u_yu_z\hat{\epsilon}_{\mathbf{k},y} + u_y^2\hat{\epsilon}_{\mathbf{k},z}) + 3d_{33}u_z^2\hat{\epsilon}_{\mathbf{k},z}]. \end{aligned} \quad (\text{B4})$$

The term inside the square bracket can be denoted as $g_j(\mathbf{k}, \mathbf{r})$ together with $\frac{1}{2}\epsilon_0\sqrt{\hbar\omega_k/2\epsilon_0V}$, then the Hamiltonian can be rewritten as

$$\begin{aligned} H_{\text{nl}} &= \sum_{j \in \{1,2\}} \int \int d\mathbf{k} d\mathbf{r} e^{-i\mathbf{k}\cdot\mathbf{r}} g_j(\mathbf{k}, \mathbf{r}) \\ &\times a_1 a_2 b_{\mathbf{k}}^\dagger e^{-i(\omega_1+\omega_2-\omega_k)t} + \text{h.c.} \end{aligned} \quad (\text{B5})$$

For a rotational symmetric ring resonator, the vectors $\mathbf{k} = (k_x, k_y, k_z)$ and $\mathbf{r} = (x, y, z)$ can be transformed to the polar coordinate $\mathbf{k} = (k\sin\theta_k\cos\phi_k, k\sin\theta_k\sin\phi_k, k\cos\theta_k)$ and cylindrical coordinate $\mathbf{r} = (r\cos\phi_r, r\sin\phi_r, h)$. Here, the coordinate (x, y, z) might be different from the (x, y, z) according to the crystal orientation. The field distribution $u(\mathbf{r})$ of mode a can be decomposed to an invariant distribution u_0 in the cross section and an angle-dependent phase $e^{im\phi_r}$ by $u(\mathbf{r}) = u_0 \widehat{e}^{im\phi_r}$, with m being the angular momentum number. In the cross section,

$$u_{x'} = e^{im\phi_r} (u_{0,x'}\cos\phi_r - u_{0,y'}\sin\phi_r), \quad (\text{B6})$$

$$u_{y'} = e^{im\phi_r} (u_{0,y'}\cos\phi_r + u_{0,x'}\sin\phi_r), \quad (\text{B7})$$

$$u_{z'} = e^{im\phi_r} u_{0,z'}. \quad (\text{B8})$$

For the plane wave in free space, there are two polarizations, with the electric field perpendicular to \mathbf{k} . These two polarizations are derived independently, denoted as $g_{\mathbf{k},1}$ and $g_{\mathbf{k},2}$, respectively. According to the wave vector $\mathbf{k} = (k\sin\theta_k\cos\phi_k, k\sin\theta_k\sin\phi_k, k\cos\theta_k)$, we can derive the vector of the two polarizations as

$$\mathbf{e}_1 = (-\cos\theta_k\cos\phi_k, -\cos\theta_k\sin\phi_k, \sin\theta_k), \quad (\text{B9})$$

$$\mathbf{e}_2 = (\sin\phi_k, -\cos\phi_k, 0), \quad (\text{B10})$$

where the \mathbf{e}_1 lies in the plane spanned by \mathbf{k} and the z' axis, and the two polarization modes share the same field amplitude $\varepsilon = \sqrt{\hbar\omega_k/2\epsilon_0V}$ in directions \mathbf{e}_1 and \mathbf{e}_2 . We should transform our coordinate to align the crystal by

$$\begin{pmatrix} x \\ y \\ z \end{pmatrix} = \begin{pmatrix} 0 & 0 & 1 \\ 0 & -1 & 0 \\ 1 & 0 & 0 \end{pmatrix} \begin{pmatrix} x' \\ y' \\ z' \end{pmatrix}. \quad (\text{B11})$$

Then we have the vector

$$\mathbf{k} = (k \sin \theta_k \cos \phi_k, k \sin \theta_k \sin \phi_k, k \cos \theta_k), \quad (\text{B12})$$

$$\mathbf{e}_1 = (\sin \theta_k, \cos \theta_k \sin \phi_k, -\cos \theta_k \cos \phi_k), \quad (\text{B13})$$

$$\mathbf{e}_2 = (0, \cos \phi_k, \sin \phi_k). \quad (\text{B14})$$

The electric fields fulfill the transformation (up to a phase $e^{im\phi_r}$)

$$u_x = e^{2im\phi_r} u_{0,x}, \quad (\text{B15})$$

$$u_y = e^{2im\phi_r} (u_{0,y} \cos \phi_r - u_{0,z} \sin \phi_r), \quad (\text{B16})$$

$$u_z = e^{2im\phi_r} (u_{0,z} \cos \phi_r + u_{0,y} \sin \phi_r), \quad (\text{B17})$$

and

$$\begin{pmatrix} u_{0,x} \\ u_{0,y} \\ u_{0,z} \end{pmatrix} = \begin{pmatrix} 0 & 0 & 1 \\ 0 & -1 & 0 \\ 1 & 0 & 0 \end{pmatrix} \begin{pmatrix} u_{0,x'} \\ u_{0,y'} \\ u_{0,z'} \end{pmatrix}. \quad (\text{B18})$$

Therefore,

$$u_x = e^{im\phi_r} u_{0,z'} \quad (\text{B19})$$

$$u_y = e^{im\phi_r} (-u_{0,y'} \cos \phi_r - u_{0,x'} \sin \phi_r) \quad (\text{B20})$$

$$u_z = e^{im\phi_r} (u_{0,x'} \cos \phi_r - u_{0,y'} \sin \phi_r). \quad (\text{B21})$$

Then we can derive the nonlinear coupling rate $g(\mathbf{k}, \mathbf{r})$ for each polarization mode as

$$\begin{aligned} g_1(\mathbf{k}, \mathbf{r}) = & \frac{1}{2} \epsilon_0 \sqrt{\frac{\hbar \omega_k}{2 \epsilon_0 V}} e^{-i(\omega_1 + \omega_2 - \omega_k)t} e^{i(m_1 + m_2)\phi_r} \\ & [3d_{31} [2u_{0,z'} (u_{0,x'} \cos \phi_r - u_{0,y'} \sin \phi_r) \sin \theta_k \\ & + u_{0,z'}^2 (-\cos \theta_k \cos \phi_k)] \\ & - 3d_{22} [2u_{0,z'} (-u_{0,y'} \cos \phi_r - u_{0,x'} \sin \phi_r) \sin \theta_k \\ & + u_{0,z'}^2 \cos \theta_k \sin \phi_k] \\ & + 3d_{22} (-u_{0,y'} \cos \phi_r - u_{0,x'} \sin \phi_r)^2 \cos \theta_k \sin \phi_k \\ & + 2d_{31} [2u_{0,z'} (-u_{0,y'} \cos \phi_r - u_{0,x'} \sin \phi_r) \\ & \times \cos \theta_k \sin \phi_k \\ & + (-u_{0,y'} \cos \phi_r - u_{0,x'} \sin \phi_r)^2 \sin \theta_k] \\ & + d_{31} [2 (-u_{0,y'} \cos \phi_r - u_{0,x'} \sin \phi_r) \\ & \times (u_{0,x'} \cos \phi_r - u_{0,y'} \sin \phi_r) \cos \theta_k \sin \phi_k \\ & + (-u_{0,y'} \cos \phi_r - u_{0,x'} \sin \phi_r)^2 (-\cos \theta_k \cos \phi_k)] \\ & + 3d_{33} (u_{0,x'} \cos \phi_r - u_{0,y'} \sin \phi_r)^2 \\ & \times (-\cos \theta_k \cos \phi_k)]. \end{aligned} \quad (\text{B22})$$

$$\begin{aligned} g_2(\mathbf{k}, \mathbf{r}) = & \frac{1}{2} \epsilon_0 \sqrt{\frac{\hbar \omega_k}{2 \epsilon_0 V}} e^{-i(\omega_1 + \omega_2 - \omega_k)t} e^{i(m_1 + m_2)\phi_r} \\ & [3d_{31} u_{0,z'}^2 \sin \phi_k - 3d_{22} u_{0,z'}^2 \cos \phi_k \\ & + 3d_{22} (-u_{0,y'} \cos \phi_r - u_{0,x'} \sin \phi_r)^2 \cos \phi_k \\ & + 2d_{31} [2u_{0,z'} (-u_{0,y'} \cos \phi_r - u_{0,x'} \sin \phi_r) \cos \phi_k] \\ & + d_{31} [2 (-u_{0,y'} \cos \phi_r - u_{0,x'} \sin \phi_r) \\ & \times (u_{0,x'} \cos \phi_r - u_{0,y'} \sin \phi_r) \cos \phi_k \\ & + (-u_{0,y'} \cos \phi_r - u_{0,x'} \sin \phi_r)^2 \sin \phi_k] \\ & + 3d_{33} (u_{0,x'} \cos \phi_r - u_{0,y'} \sin \phi_r)^2 \sin \phi_k]. \end{aligned} \quad (\text{B23})$$

For the TE mode, we have the most electric field oscillating in the x direction for $\phi_r = 0$, thus $u_{0,z'}, u_{0,y'} \approx 0$, and

$$\begin{aligned} g_1(\mathbf{k}, \mathbf{r}) = & \frac{1}{2} \epsilon_0 \sqrt{\frac{\hbar \omega_k}{2 \epsilon_0 V}} e^{-i(\omega_1 + \omega_2 - \omega_k)t} e^{i(m_1 + m_2)\phi_r} e^{-i\mathbf{k}\cdot\mathbf{r}} \\ & [3d_{22} \sin^2 \phi_r \cos \theta_k \sin \phi_k + 2d_{31} \sin^2 \phi_r \sin \theta_k \\ & - d_{31} (2 \sin \phi_r \cos \phi_r \cos \theta_k \sin \phi_k \\ & + \sin^2 \phi_r \cos \theta_k \cos \phi_k) \\ & - 3d_{33} \cos^2 \phi_r \cos \theta_k \cos \phi_k] u_{0,x'}^2. \end{aligned} \quad (\text{B24})$$

$$\begin{aligned} g_2(\mathbf{k}, \mathbf{r}) = & \frac{1}{2} \epsilon_0 \sqrt{\frac{\hbar \omega_k}{2 \epsilon_0 V}} e^{-i(\omega_1 + \omega_2 - \omega_k)t} e^{i(m_1 + m_2)\phi_r} e^{-i\mathbf{k}\cdot\mathbf{r}} \\ & [3d_{22} \sin^2 \phi_r \cos \phi_k + d_{31} (-2 \sin \phi_r \cos \phi_r \cos \phi_k \\ & + \sin^2 \phi_r \sin \phi_k) + 3d_{33} \cos^2 \phi_r \sin \phi_k] u_{0,x'}^2. \end{aligned} \quad (\text{B25})$$

Considering that the d_{33} of LN is much larger than d_{22} and d_{31} , the local coupling rates of the two polarizations reduce to

$$\begin{aligned} g_1(\mathbf{k}, \mathbf{r}) = & -\frac{3}{2} \epsilon_0 \sqrt{\frac{\hbar \omega_k}{2 \epsilon_0 V}} e^{-i(\omega_1 + \omega_2 - \omega_k)t} e^{i(m_1 + m_2)\phi_r} e^{-i\mathbf{k}\cdot\mathbf{r}} \\ & \times d_{33} \cos^2 \phi_r \cos \theta_k \cos \phi_k u_{0,x'}^2, \end{aligned} \quad (\text{B26})$$

$$\begin{aligned} g_2(\mathbf{k}, \mathbf{r}) = & \frac{3}{2} \epsilon_0 \sqrt{\frac{\hbar \omega_k}{2 \epsilon_0 V}} e^{-i(\omega_1 + \omega_2 - \omega_k)t} e^{i(m_1 + m_2)\phi_r} e^{-i\mathbf{k}\cdot\mathbf{r}} \\ & \times d_{33} \cos^2 \phi_r \sin \phi_k u_{0,x'}^2. \end{aligned} \quad (\text{B27})$$

For collection from the vertical direction, the local radiated power is proportional to $|g_i(\mathbf{k}, \mathbf{r})|^2$ according to Eqs. (A24)

and (A25). Eventually, we have

$$P_{\text{out}} \propto \cos^4 \phi_r, \quad (\text{B28})$$

which explains the observed radiation pattern in Fig. 2(b) of the main text.

APPENDIX C: DEVICE PARAMETERS

1. Fabrication process

Device *A* is fabricated with 600-nm-thick *x*-cut thin-film LN on a silica substrate (NanoLN). Device *B* is fabricated with a 500-nm-thick *x*-cut thin-film LN on a sapphire substrate (NanoLN). The device patterns are defined by a hydrogen silses-quioxane (HSQ) resist via electron-beam lithography, and then transferred to LN through the optimized Ar⁺-etching process by an inductively coupled plasma reactive ion-etching (ICP RIE) tool. As shown in Figs. 5(a) and 5(b), a thickness of 220 nm of LN is etched, the angle of the waveguide sidewall is around 55°. For device *A*, the radius of the microring is 100 μm, and the widths of the coupling waveguide and microring cavity are both 3 μm. The coupling gap between the waveguide and microring is about 1160 nm. For device *B*, the radius of the microring is 70 μm, and the widths of the coupling waveguide and microring cavity are 1.72 and 1.8 μm, respectively. The coupling gap between the waveguide and microring is about 600 nm.

We use fiber lens to inject the laser into the chip, the on-chip devices could be characterized, with an estimated single-side coupling efficiency of 15.6%. The cavity transmission spectra as well as the fitting results of devices *A* and *B* are plotted in Figs. 5(c) and 5(d). The loaded *Q* factors of devices *A* and *B* are 8.05×10^5 and 6.99×10^4 , respectively. We measure the dependence of loaded quality factor on the coupling gap on by arrays of devices

and confirm that both device *A* and device *B* are in the undercoupled regime. Therefore, their intrinsic *Q* factors are deduced to be 2.11×10^6 and 1.85×10^5 .

2. Transmission and NOR spectra

With the optical setup shown in the main text, the NOR is collected by an objective lens with a NA = 0.42 and a working distance around 2 cm. In Figs. 2(d) and 2(e), we show the NOR signal as well as the transmission spectra of device *A*. It should be noted that the mode numbers in Fig. 2(e) is about 5 times greater than the peak numbers in Fig. 2(d). As shown in Fig. 6(a), we cascade five microrings coupled with the same straight bus waveguide. The five microrings vary slightly in the radius and width of the coupling gap. In this way, resonance modes of different microrings would not overlap with each other, while they have nearly the same free spectra range $\text{FSR} \approx 1.62 \text{ nm}$ in the telecom band [marked with blue arrows in Fig. 6(c)]. In our experiment, we collect only the signal of a small part of one microring [blue circle in Fig. 2(b)] from the objective lens. The distance between adjacent microrings is large enough, so that the NOR signal from the other four microrings would not be collected. Thus, we observe five dips in the transmission spectrum and one peak in the NOR signal spectrum within one FSR, as shown clearly in Figs. 6(b) and 6(c).

The visible input laser used for inducing DFG is generated by a PPLN frequency doubler pumped by a continuous-wave telecom laser. A half-wave plate is applied to control the polarization of visible pump, which could tune the nonlinear interaction to match the strongest nonlinear susceptibility d_{33} by optimizing the signal of DFG.

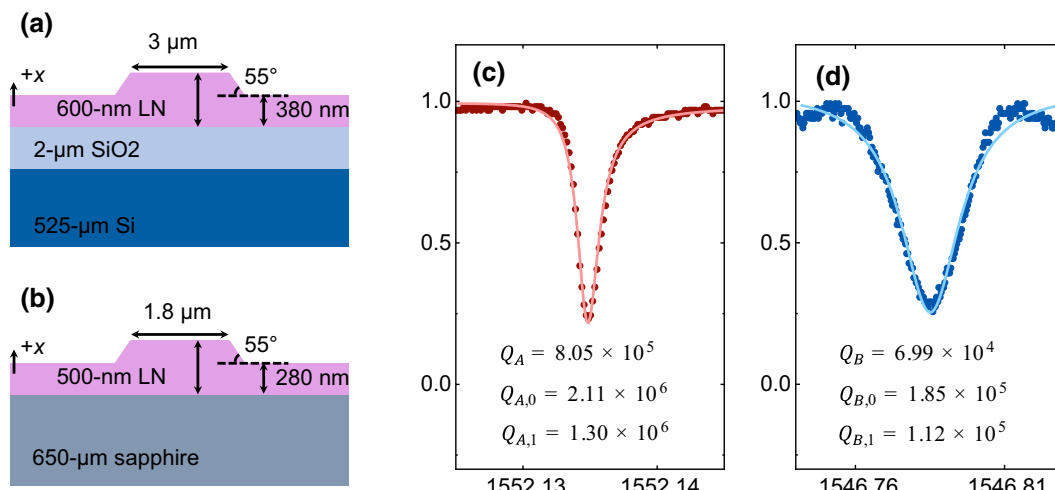


FIG. 5. (a),(b) Cross sections of devices *A* and *B*, which are fabricated with *x*-cut thin-film LN on different substrates. (c),(d) Transmission spectra and corresponding fitting results of devices *A* and *B*, respectively.

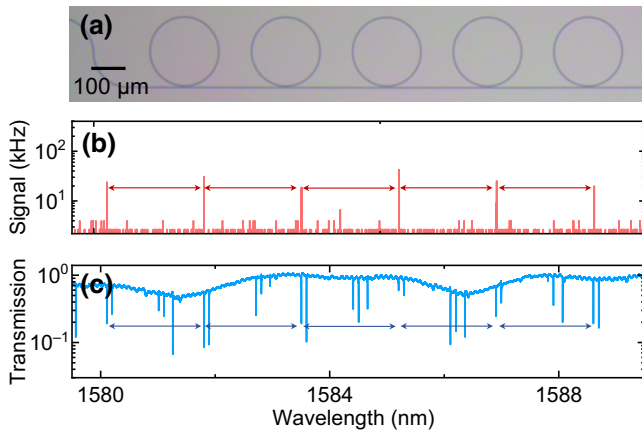


FIG. 6. (a) Microscope image of device *A*. (b),(c) NOR signal and corresponding transmission spectra. The blue and red arrows represent the FSR of device *A* in the telecom band.

- scale: integrated photonics meets integrated phononics, *Optica* **6**, 213 (2019).
- [12] C. Xiong, W. H. P. Pernice, X. Sun, C. Schuck, K. Y. Fong, and H. X. Tang, Aluminum nitride as a new material for chip-scale optomechanics and nonlinear optics, *New J. Phys.* **14**, 095014 (2012).
 - [13] H. Jung, C. Xiong, K. Y. Fong, X. Zhang, and H. X. Tang, Optical frequency comb generation from aluminum nitride microring resonator, *Opt. Lett.* **38**, 2810 (2013).
 - [14] M. Soltani, R. Soref, T. Palacios, and D. Englund, AlGaN/AlN integrated photonics platform for the ultraviolet and visible spectral range, *Opt. Express* **24**, 25415 (2016).
 - [15] X. Guo, C. Zou, and H. Tang, Second-harmonic generation in aluminum nitride microrings with 2500% W conversion efficiency, *Optica* **3**, 1126 (2016).
 - [16] J.-Q. Wang, Y.-H. Yang, M. Li, X.-X. Hu, J. B. Surya, X.-B. Xu, C.-H. Dong, G.-C. Guo, H. X. Tang, and C.-L. Zou, Efficient Frequency Conversion in a Degenerate $\chi^{(2)}$ Microresonator, *Phys. Rev. Lett.* **126**, 133601 (2021).
 - [17] A. W. Bruch, C. Xiong, B. Leung, M. Poot, J. Han, and H. X. Tang, Broadband nanophotonic waveguides and resonators based on epitaxial GaN thin films, *Appl. Phys. Lett.* **107**, 141113 (2015).
 - [18] M. S. Mohamed, A. Simbula, J.-F. Carlin, M. Minkov, D. Gerace, V. Savona, N. Grandjean, M. Galli, and R. Houdré, Efficient continuous-wave nonlinear frequency conversion in high-Q gallium nitride photonic crystal cavities on silicon, *APL Photon.* **2**, 031301 (2017).
 - [19] E. Stassen, M. Pu, E. Semenova, E. Zavarin, W. Lundin, and K. Yvind, High-confinement gallium nitride-on-sapphire waveguides for integrated nonlinear photonics, *Opt. Lett.* **44**, 1064 (2019).
 - [20] Y. Zheng, C. Sun, B. Xiong, L. Wang, Z. Hao, J. Wang, Y. Han, H. Li, J. Yu, and Y. Luo, Integrated gallium nitride nonlinear photonics, *Laser Photon. Rev.* **16**, 2100071 (2022).
 - [21] P. S. Kuo, J. Bravo-Abad, and G. S. Solomon, Second-harmonic generation using -quasi-phasematching in a GaAs whispering-gallery-mode microcavity, *Nat. Commun.* **5**, 3109 (2014).
 - [22] L. Midolo, T. Pregnolato, G. Kiršansk, and S. Stobbe, Soft-mask fabrication of gallium arsenide nanomembranes for integrated quantum photonics, *Nanotechnology* **26**, 484002 (2015).
 - [23] C. P. Dietrich, A. Fiore, M. G. Thompson, M. Kamp, and S. Höfling, GaAs integrated quantum photonics: Towards compact and multi-functional quantum photonic integrated circuits, *Laser Photon. Rev.* **10**, 870 (2016).
 - [24] J. Lin, N. Yao, Z. Hao, J. Zhang, W. Mao, M. Wang, W. Chu, R. Wu, Z. Fang, L. Qiao, W. Fang, F. Bo, and Y. Cheng, Broadband Quasi-Phase-Matched Harmonic Generation in an On-Chip Monocrystalline Lithium Niobate Microdisk Resonator, *Phys. Rev. Lett.* **122**, 173903 (2019).
 - [25] A. Pan, C. Hu, C. Zeng, and J. Xia, Fundamental mode hybridization in a thin film lithium niobate ridge waveguide, *Opt. Express* **27**, 35659 (2019).
 - [26] X. Liu, X. Yan, Y. Liu, H. Li, Y. Chen, and X. Chen, Tunable single-mode laser on thin film lithium niobate, *Opt. Lett.* **46**, 5505 (2021).

- [27] Y. Qi and Y. Li, Integrated lithium niobate photonics, *Nanophotonics* **9**, 1287 (2020).
- [28] J. Zhou, Y. Liang, Z. Liu, W. Chu, H. Zhang, D. Yin, Z. Fang, R. Wu, J. Zhang, W. Chen, Z. Wang, Y. Zhou, M. Wang, and Y. Cheng, On-chip integrated waveguide amplifiers on erbium-doped thin-film lithium niobate on insulator, *Laser Photon. Rev.* **15**, 2100030 (2021).
- [29] G.-T. Xue, Y.-F. Niu, X. Liu, J.-C. Duan, W. Chen, Y. Pan, K. Jia, X. Wang, H.-Y. Liu, Y. Zhang, P. Xu, G. Zhao, X. Cai, Y.-X. Gong, X. Hu, Z. Xie, and S. Zhu, Ultra-bright Multiplexed Energy-Time-Entangled Photon Generation from Lithium Niobate on Insulator Chip, *Phys. Rev. Appl.* **15**, 064059 (2021).
- [30] J. Lin, F. Bo, Y. Cheng, and J. Xu, Advances in on-chip photonic devices based on lithium niobate on insulator, *Photon. Res.* **8**, 1910 (2020).
- [31] S. Yuan, Y. Wu, Z. Dang, C. Zeng, X. Qi, G. Guo, X. Ren, and J. Xia, Strongly Enhanced Second Harmonic Generation in a Thin Film Lithium Niobate Heterostructure Cavity, *Phys. Rev. Lett.* **127**, 153901 (2021).
- [32] X. Liu, P. Ying, X. Zhong, J. Xu, Y. Han, S. Yu, and X. Cai, Highly efficient thermo-optic tunable micro-ring resonator based on an LNOI platform, *Opt. Lett.* **45**, 6318 (2020).
- [33] J. Lu, M. Li, C.-L. Zou, A. Al Sayem, and H. X. Tang, Toward 1% single-photon anharmonicity with periodically poled lithium niobate microring resonators, *Optica* **7**, 1654 (2020).
- [34] J. Lu, A. Al Sayem, Z. Gong, J. B. Surya, C.-L. Zou, and H. X. Tang, Ultralow-threshold thin-film lithium niobate optical parametric oscillator, *Optica* **8**, 539 (2021).
- [35] J. Lu, J. B. Surya, X. Liu, A. W. Bruch, Z. Gong, Y. Xu, and H. X. Tang, Periodically poled thin-film lithium niobate microring resonators with a second-harmonic generation efficiency of 250,000%/W, *Optica* **6**, 1455 (2019).
- [36] S.-B. Lee, J. Yang, S. Moon, J.-H. Lee, K. An, J.-B. Shim, H.-W. Lee, and S. W. Kim, Universal output directionality of single modes in a deformed microcavity, *Phys. Rev. A* **75**, 011802 (2007).
- [37] X.-F. Jiang, C.-L. Zou, L. Wang, Q. Gong, and Y.-F. Xiao, Whispering-gallery microcavities with unidirectional laser emission, *Laser Photon. Rev.* **10**, 40 (2016).
- [38] S. Kim, D. A. Westly, B. J. Roxworthy, Q. Li, A. Yulaev, K. Srinivasan, and V. A. Aksyuk, Photonic waveguide to free-space Gaussian beam extreme mode converter, *Light Sci. Appl.* **7**, 72 (2018).
- [39] G. Calafiole, A. Koshelev, S. Dhuey, A. Goltsov, P. Sasorov, S. Babin, V. Yankov, S. Cabrini, and C. Peroz, Holographic planar lightwave circuit for on-chip spectroscopy, *Light Sci. Appl.* **3**, e203 (2014).
- [40] Y. Meng, Z. Liu, Z. Xie, R. Wang, T. Qi, F. Hu, H. Kim, Q. Xiao, X. Fu, Q. Wu, S.-H. Bae, M. Gong, and X. Yuan, Versatile on-chip light coupling and (de)multiplexing from arbitrary polarizations to controlled waveguide modes using an integrated dielectric metasurface, *Photon. Res.* **8**, 564 (2020).
- [41] Y. J. Ding, S. J. Lee, and J. B. Khurgin, Transversely Pumped Counterpropagating Optical Parametric Oscillation and Amplification, *Phys. Rev. Lett.* **75**, 429 (1995).
- [42] M. T. Hummon, S. Kang, D. G. Bopp, Q. Li, D. A. Westly, S. Kim, C. Fredrick, S. A. Diddams, K. Srinivasan, V. Aksyuk, and J. E. Kitching, Photonic chip for laser stabilization to an atomic vapor with 10^{-11} instability, *Optica* **5**, 443 (2018).
- [43] R. J. Niffenegger, J. Stuart, C. Sorace-Agaskar, D. Kharas, S. Bramhavar, C. D. Bruzewicz, W. Loh, R. T. Maxson, R. McConnell, D. Reens, G. N. West, J. M. Sage, and J. Chiaverini, Integrated multi-wavelength control of an ion qubit, *Nature* **586**, 538 (2020).
- [44] L. Stern, J. R. Stone, S. Kang, D. C. Cole, M.-G. Suh, C. Fredrick, Z. Newman, K. Vahala, J. Kitching, S. A. Diddams, and S. B. Papp, Direct Kerr frequency comb atomic spectroscopy and stabilization, *Sci. Adv.* **6**, eaax6230 (2020).
- [45] S. Gundavarapu, G. M. Brodnik, M. Puckett, T. Huffman, D. Bose, R. Behunin, J. Wu, T. Qiu, C. Pinho, N. Chauhan, J. Nohava, P. T. Rakich, K. D. Nelson, M. Salit, and D. J. Blumenthal, Sub-hertz fundamental linewidth photonic integrated Brillouin laser, *Nat. Photon.* **13**, 60 (2019).
- [46] J. Xie, J.-Q. Wang, Z.-B. Wang, X.-X. Hu, X. Guo, R. Niu, J. B. Surya, J.-Z. Zhang, C.-H. Dong, G.-C. Guo, H. X. Tang, and C.-L. Zou, Infrared laser locking to a rubidium saturated absorption spectrum via a photonic chip frequency doubler, *Opt. Lett.* **44**, 1150 (2019).
- [47] T. Tan, Z. Yuan, H. Zhang, G. Yan, S. Zhou, N. An, B. Peng, G. Soavi, Y. Rao, and B. Yao, Multispecies and individual gas molecule detection using Stokes solitons in a graphene over-modal microresonator, *Nat. Commun.* **12**, 6716 (2021).
- [48] C. Bao, Z. Yuan, L. Wu, M.-G. Suh, H. Wang, Q. Lin, and K. J. Vahala, Architecture for microcomb-based GHz-mid-infrared dual-comb spectroscopy, *Nat. Commun.* **12**, 6573 (2021).
- [49] P. K. Tien, R. Ulrich, and R. J. Martin, Optical second harmonic generation in form of coherent Cerenkov radiation from a thin waveguide, *Appl. Phys. Lett.* **17**, 447 (1970).